Tuning of Structure, Morphology and Magnetism in Postperovskite Oxide Solid Solutions

Cite As: Hirai, S, Sanehira, T, Nishiyama, N, Irifune, T, Klemme, S, Bromiley, G & Attfield, JP 2011, 'Tuning of Structure, Morphology and Magnetism in Postperovskite Oxide Solid Solutions' *Chemistry of Materials*, vol 23, no. 1, pp. 114-121.

DOI: 10.1021/cm102660q

Tuning of structure, morphology and magnetism in post-perovskite oxide solid solutions

Shigeto Hirai[*], Takeshi Sanehira[**], Norimasa Nishiyama[**], Tetsuo Irifune[**], Stephan Klemme[***], Geoffrey Bromiley[*] and J. Paul Attfield[****]

[*]Centre for Science at Extreme Conditions and School of Geosciences, University of Edinburgh, Mayfield Road, Edinburgh EH9 3JZ, UK

[**] Geodynamics Research Center, Ehime University, 2-5 Bunkyo-cho, Matsuyama, Ehime 790-8577, Japan

[***] Institut für Mineralogie, Corrensstr. 24, Universität Münster, 48149 Münster, Germany

[****] Centre for Science at Extreme Conditions and School of Chemistry, University of Edinburgh, Mayfield Road, Edinburgh EH9 3JZ, UK

Abstract: High-quality polycrystalline samples of post-perovskite type $CaIr_{1-x}Pt_xO_3$ solid solutions (x = 0.3, 0.5, 0.7) and $CaIr_{0.5}Rh_{0.5}O_3$ have been synthesised at a pressure of 15 GPa, and their structures and properties are compared to those of $CaIrO_3$. Substantial [100] grain growth is observed in all samples leading to pronounced texture even in powdered materials. Small changes in the lattice constants and octahedral distortions are observed in the $CaIr_{1-x}Pt_xO_3$ series, consistent with a reduction in Jahn-Teller activity. $CaIrO_3$ is semiconducting and shows temperature-independent paramagnetism, and an ordered moment of 0.04 μ_B below a 108 K magnetic transition. Doping with Pt or Rh induces Curie-Weiss paramagnetism and suppresses the magnetic transition, to zero for ~40% Pt doping. The anisotropic structure and morphology of $CaIrO_3$ combined with the Ir^{4+} spin-orbit coupling result in a large magnetic anisotropy constant of 1.77×10^6 Jm^{-3}, comparable to values for permanent magnet materials.

I. Introduction

Since the discovery of the perovskite to post-perovskite transition in $MgSiO_3$ in a laser-heated diamond anvil cell[1], wide attention has been focussed on the post-perovskite phase of $MgSiO_3$. This is because the post-perovskite phase is likely to play a key role in processes occurring in Earth's lower mantle, and the perovskite to post-perovskite transition can explain many features of the D" seismic discontinuity there. While it is important to conduct further studies on $MgSiO_3$, this post-perovskite phase cannot be quenched to ambient conditions; this is also the case for the post-perovskite type transition metal oxides Fe_2O_3 [2] and Mn_2O_3 [3]. Thus, it is useful to investigate the materials properties of structural analogues of the $MgSiO_3$ post-perovskite that are quenchable to ambient conditions. The electronic and magnetic properties of transition metal analogues are also of interest as post-perovskite type oxides are rare and their physical properties have not been extensively explored.

The post-perovskite phase of $MgSiO_3$ adopts the layered $CaIrO_3$-type structure containing corner-linked chains of edge-sharing octahedra (Fig.1). Four quenchable $CaIrO_3$-type oxides have been reported to date: $CaIrO_3$[4], $CaPtO_3$ [5], $CaRhO_3$ [6] and $CaRuO_3$ [7]. Polycrystalline $CaIrO_3$ can be synthesized at ambient pressure from binary oxides heated to 1273 K in an evacuated silica tube, and single crystals of $CaIrO_3$ were synthesized at 1223 K using a $CaCl_2$ flux.[4] The other three oxides were obtained using a multi-anvil apparatus to achieve high pressure (P) and temperature (T) conditions; $CaPtO_3$ (4GPa, 1073K),[5] $CaRhO_3$ (6GPa, 1473K) [6] and $CaRuO_3$ (23GPa, 1223K). [7] Further studies on these materials have revealed post-perovskite to perovskite structural phase transitions at high P-T. The post-perovskite phase of $CaIrO_3$ transforms to the perovskite structure at 2GPa, 1673K[8] and this transformation was also observed for $CaRhO_3$ (6GPa, 1873K) and $CaRuO_3$ (23GPa, 1343K), while $CaPtO_3$ remained in the post-perovskite structure at higher temperatures[9]. The former observations show that the perovskite type is the high temperature phase for these $CaMO_3$ post-perovskites, and this was supported by a Raman spectroscopy study of $CaIrO_3$ up to 30GPa [10] and a synchrotron X-ray diffraction of $CaPtO_3$ up to 40GPa [11] which show that the phase transition from post-perovskite to perovskite transition does not occur at room temperature.

The presence of transition metal ions in the above $CaMO_3$ post-perovskites suggests that such phases might have interesting electronic or magnetic properties. A study of $Ca_{1-x}Na_xIrO_3$

solid solutions (synthesized at 4GPa, 1073K)[12] revealed a metal-insulator transition at x = 0.37. To investigate such properties further, we have explored the $CaIr_{1-x}Pt_xO_3$ series and the synthesis, structural and physical properties of these solid solutions are reported here. We also demonstrate that $CaIr_{1-x}Rh_xO_3$ materials are accessible as we report the x = 0.5 member of this series.

II. Experimental Section

Polycrystalline samples of $CaIrO_3$ post-perovskite were synthesized by solid state reaction from CaO and IrO_2. CaO powder was prepared from $CaCO_3$ by heating in air at 1000 °C for 24 hrs. Well-ground mixtures of the starting materials in the stoichiometric ratio were sealed in an evacuated silica tube, and heated in air at 1273K over 20 hrs. $CaIrO_3$ post-perovskite single crystals were synthesized by a flux method [4].

Polycrystalline samples of $CaIr_{1-x}Pt_xO_3$ and $CaIr_{0.5}Rh_{0.5}O_3$ were synthesized at high pressure-temperature conditions. $CaIr_{1-x}Pt_xO_3$ (x = 0.3, 0.5, 0.7) were synthesized by solid-state reaction from CaO, IrO_2, and PtO_2 powders. Well-ground mixtures of the starting material in a stoichiometric molar ratio were placed into an Au capsule (ϕ =2.5 mm) sandwiched by BN composite disks (ϕ =2.7 mm). $CaIr_{0.5}Rh_{0.5}O_3$ was synthesized by solid-state reaction from CaO, IrO_2, and Rh_2O_3, with $KClO_4$ as an oxidizer. A well-ground mixture of the starting materials at a ratio of 1/0.5/0.5/4.07 (Ca/Ir/Rh/O) was placed into an Au capsule (ϕ =2.5 mm) sandwiched by MgO disks (ϕ =2.7 mm), to avoid sample reduction. The capsules were heated in a multi-anvil apparatus at 1573 K and 15GPa pressure for 40 min, followed by rapid quenching to ambient temperature, and then release of pressure. A pressure of 15GPa was used to ensure that homogenous solid solutions were formed as reactions at 3 and 10 GPa gave samples with a range of Ir/Pt ratios and containing IrO_2 and Pt secondary phases. Dense black pellets were obtained and that of $CaIr_{0.5}Rh_{0.5}O_3$ was washed with distilled water to remove KCl.

Powdered samples were investigated by powder X-ray diffraction (XRD) using a Bruker D8 diffractometer in reflection geometry with monochromated Cu Kα1 radiation. Two patterns were collected for each sample – one from the loosely packed powder and the other from the powder sieved onto a sample holder covered by a thin layer of organic grease, to minimise preferred orientation of crystallites. The GSAS software was used for Rietveld refinement of the crystal structure and texture analysis. [13] Scanning electron microscopy with energy dispersive X-ray analysis (SEM/EDX) was conducted on a polished surface of selected samples using a Phillips XL30CP, with PGT Spirit X-ray analysis, using an acceleration voltage of 20 kV.

Electrical resistivities of rectangular pellets were studied by a four-point probe method with a gauge current of 0.99 mA. Electrical contacts were made from Cu wires and silver paste.

Magnetisations were measured using a Quantum Design MPMS SQUID magnetometer. Zero field- and field-cooled (ZFC and FC) measurements were made with a field of 100 Oe after cooling the sample to 5 K. Ambient condition Raman spectra on $CaIr_{1-x}Pt_xO_3$ (x = 0.3, 0.5, 0.7) and $CaIr_{0.5}Rh_{0.5}O_3$ were collected using a Jobin Yvon LabRAM instrument (λ = 632.8 nm).

III. Results

A Structure and Morphology

XRD patterns (Fig. 2) demonstrate that the recovered $CaIr_{1-x}Pt_xO_3$ (x = 0, 0.3, 0.5, 0.7) and $CaIr_{0.5}Rh_{0.5}O_3$ samples contain post-perovskites with traces of secondary phases in some cases. All of the major XRD peaks are indexed by the $CaIrO_3$-type cell with orthorhombic space group *Cmcm*. The Raman spectra are similar to that for $CaIrO_3$ and the shifts of the five primary Raman modes of $CaIr_{1-x}Pt_xO_3$ series (Table 1) confirm that solid solutions are present. The ν_4 Raman mode is not observed in $CaIrO_3$ but appears around 563 cm^{-1} for all the Pt or Rh doped samples.

The morphologies and stoichiometries of the samples were examined by SEM/EDX analysis for $CaIr_{0.5}Rh_{0.5}O_3$ and by using an electron microprobe for $CaIr_{1-x}Pt_xO_3$ (x = 0, 0.3, 0.5, 0.7). Traces of additional elements were not detected for any of the samples in the EDX patterns and the stoichiometries were confirmed as being the same as the nominal compositions. The crystallites show a needle-like morphology in all samples. The growth of needle-like grains elongated in the *a*-axis direction was previously reported for $CaIrO_3$ and $CaPtO_3$.[2,3,14] The mean grain size varies in the range 1-8μm between samples as shown in the micrographs in Fig. 3 and as summarised in Table 2. Large grains are also observed for polycrystalline $CaIrO_3$ post-perovskite, prepared at ambient pressures and temperatures around 1273 K. For the $CaIr_{1-x}Pt_xO_3$ samples prepared at, 15GPa and 1573 K, grain growth is greater for x = 0.5 than for x = 0.3 and 0.7 suggesting that the minimum melting point in the $CaIr_{1-x}Pt_xO_3$ series is near x = 0.5.

Initial Rietveld fits to the XRD profiles showed that strong textures were present in the loosely packed powders and so another pattern was collected from each sample sieved onto a greased surface to minimise this effect. Large differences between the two patterns for each sample are evident in Fig. 2. Fits to the greased samples were used to refine the crystal structure parameters, giving the results shown in Table 2. The variation of lattice parameters with composition in the $CaIr_{1-x}Pt_xO_3$ series is shown in Fig. 4, taking results for $CaPtO_3$ from ref. 5. It is notable that the *a*- and *b*-axis lengths change linearly with composition, whereas the *c*-axis shows curvature and lies below the values expected by linear interpolation between the end-members for $0 < x < 1$. This leads to the same trend in the cell volume. This non-linearity

suggests that some local ordering of Ir/Pt occurs within the chains of corner-sharing octahedra along the *c*-direction of the crystal structure (Fig. 1).

The Ir/Pt/RhO_6 octahedra show a tetragonal compression in all $CaIr_{1-x}Pt_xO_3$ structures, and in $CaIr_{0.5}Rh_{0.5}O_3$, with two short M-O1 (1.91-1.99 Å) and four long M-O2 (2.04-2.09 Å) bonds (Table 2). This is not consistent with a Jahn-Teller distortion of low spin $5d^5$ Ir^{4+}, as tetragonal elongation is needed to break the electronic degeneracy. The connectivity of the post-perovskite structure provides a likely explanation. Applying the bond valence principle that the summed valences of the bonds around a cation or anion should equal the formal valence, gives M-O1 and M-O2 valences of 12/17 (≈0.71) and 11/17 (≈0.65) respectively, showing that the M-O1 bonds are expected to be slightly stronger and shorter than the M-O2. These values compare well to bond valences in Table 2 calculated from the standard function $\exp((d_i-d_0)/B)$ and parameters, [16] where d_i is the bond distance, d_0 is a constant for a particular atom pair and B = 0.37 Å. Appropriate averages of d_0 constants were used for Ir/Pt and Ir/Rh solid solutions and the M site Bond Valence Sums (BVS's) are close to the expected +4 value. The anisotropy of the structure also results in strained CaO_8 polyhedra, with BVS's between 2.1 and 2.4. Hence, the primary octahedral distortion in the $CaMO_3$ post-perovskites is driven by the anisotropic bonding network rather than by electronic instabilities of the d-electron configuration. However, a small electronic influence is evident by calculating the octahedral distortion parameter $\Delta d = 1/6\{2(d_1-d)^2+4(d_2-d)^2\}/d^2$ (d_1: M-O1 bond distance, d_2: M-O2 bond distance, d: average M-O distance)[15]. Fig. 4(e) shows that Δd decreases across the $CaIr_{1-x}Pt_xO_3$ series as the triply degenerate ground state of low spin $5d^5$ Ir^{4+} is replaced by non-degenerate $5d^6$ Pt^{4+}. No systematic changes in the O-M-O angles or M-O-M angles (Table 2) are evident in the $CaIr_{1-x}Pt_xO_3$ series.

To obtain morphological information from the XRD patterns of loosely packed powders, the crystal structure parameters were fixed at the values obtained from the greased samples, and the intensities were Rietveld-fitted by varying the six ODF (Orientation Density Function) coefficients that describe a cylindrical symmetry sample texture up to 4^{th} order. [16] This gave a good fit to the peak intensities as shown in Fig. 2. The orientation densities derived from the refined ODF parameters are shown in Fig. 5. These show the density of crystallites with plane (hkl) at an angle ψ to the sample plane, relative to the average (untextured) value of 1.0. In all samples the maximum density for (100) is at ψ = 90°, confirming that the crystallographic a-axis is parallel to the long dimension of the needle-like crystals. The (010) and (001) densities are consequently both peaked at ψ = 0 but a systematic change from (001) to (010) density is observed as x increases from x = 0 to 0.7. This shows that Pt substitution favours (001) over (010) growth. The magnitudes of the orientation density maxima in the $CaIr_{1-x}Pt_xO_3$ series correlate well

with the grain sizes observed by SEM. The large grain $CaIrO_3$ and $CaIr_{0.5}Pt_{0.5}O_3$ show maximum densities of near 3, whereas the smaller-grained $CaIr_{0.7}Pt_{0.3}O_3$ and $CaIr_{0.3}Pt_{0.7}O_3$ have density maxima of 1.4 and 2.1 respectively. However, the $CaIr_{0.5}Rh_{0.5}O_3$ sample shows the most extreme texture with an (001) density of 4.0 at $\psi = 0$.

B Electronic and Magnetic Properties

The temperature dependences of electrical resisitivity for $CaIrO_3$, $CaIr_{0.5}Pt_{0.5}O_3$ and $CaIr_{0.5}Rh_{0.5}O_3$ are shown in Fig. 6. The samples are narrow bandgap semiconductors with bandgap energies of 34-150 meV (Table 3) estimated from the 290 K gradient of Arrhenius plots.

Fig. 7 shows the temperature dependence of magnetic susceptibility for the five samples. A ferromagnetic transition, marked by an upturn in magnetisation and divergence of zero-field and field cooled susceptibilities, is observed for $CaIrO_3$ at T_C = 108 K which is comparable to a previously reported value.[12] Transitions are seen at the same temperature for all the $CaIr_{1-x}Pt_xO_3$ solid solutions showing that traces of $CaIrO_3$ are present, although these were not observed in the EDX analyses. The intrinsic transition is suppressed to 20 K for x = 0.3 and is not observed down to 5 K for the x = 0.5 and 0.7 samples. $CaIr_{0.5}Rh_{0.5}O_3$ shows the ferromagnetic transition at 40 K. Hence both Pt and Rh substitutions suppress the magnetic transition in $CaIrO_3$ with a more rapid suppression by diamagnetic Pt^{4+} than by magnetic Rh^{4+}.

The 150-300 K inverse susceptibilities are shown in the insets to Fig. 7. $CaIrO_3$ shows temperature-independent paramagnetism over this range but the other samples have non-linear susceptibilities. These were fitted using the equation $1/\chi = [\alpha + C/T-\theta]^{-1}$ which combines temperature-independent and Curie-Weiss terms. The fitted curves are shown on Fig. 7 and the derived parameters are in Table 3. These show that $CaIrO_3$ appears to be close to a metal-insulator transition, as it shows only temperature-independent paramagnetic behaviour at high temperatures despite appearing non-metallic. Doping with Pt suppresses the near-metallic behaviour as the resistivity increases by six orders of magnitude for x = 0.5, decreases the temperature-independent paramagnetism, and gives rise to local moments, although Pt^{4+} is diamagnetic. These follow Curie-Weiss behaviour with an effective paramagnetic moment of ~0.5 μ_B/formula unit and the positive Weiss constants evidence ferromagnetic exchange interactions between spins. In contrast, $CaIr_{0.5}Rh_{0.5}O_3$ has a small negative θ, although this is almost within error of zero.

Magnetisation-field data for $CaIrO_3$, $CaIr_{0.7}Pt_{0.3}O_3$ and $CaIr_{0.5}Rh_{0.5}O_3$ are shown in Fig. 8. Ferromagnetic hysteresis loops are observed for the former two materials but $CaIr_{0.5}Rh_{0.5}O_3$ appears to have only short range ferromagnetic interactions. $CaIrO_3$ is an unusually hard magnetic

oxide, with a large magnetic anisotropy and a coercive field of H_c = 3.4T at 5K for the present sample. The thermal evolution of the hysteresis loop is also shown in Fig. 8(a). The variation of the coercive field with temperature (Fig. 9) was fitted with the equation[17]: $H_c = 2\alpha K/M_s[1-(T/T_C)^{1/2}]$ where $\alpha = 0.48$, and the fitted uniaxial anisotropy constant is $K = 1.77 \times 10^6$ Jm^{-3}. This is comparable to the value of 5×10^6 Jm^{-3} for $Nd_2Fe_{14}B$ which is a widely used permanent magnet material.[18, 19] The large crystal field and the strong spin-orbital coupling of Ir^{4+} ($5d^5$), as found in a recent study on Sr_2IrO_4,[19] and the anisotropic crystal structure and morphology of $CaIrO_3$ are all likely contributors to this exceptionally high coercivity for a magnetic oxide. Substitution of 30% Pt for Ir dilutes the magnetic interactions and decreases the saturated magnetisation from 0.040 μ_B/formula unit for $CaIrO_3$ to 0.024 μ_B/formula unit, while the 5K coercive field drops to 0.46T.

IV. Discussion

To date, the only quenchable oxides having the post-perovskite ($CaIrO_3$) structure are $CaMO_3$ for M = Ru, Rh, Ir and Pt. These M^{4+} cations are very similar, having a narrow range of ionic radii (0.60-0.625 Å)[20] and large octahedral crystal field stabilisation energies resulting from their low spin d^n (n = 4-6) electron configurations. A recent DFT study[15] of $CaRhO_3$ suggested that metal-metal bonding in the chains of edge-shared octahedra parallel to the *a*-axis, as found in the rutile types RuO_2[21], IrO_2[22], RhO_2[15,16] and ReO_2,[23] also plays a role. This may account for the ambient pressure stability of post-perovskite $CaIrO_3$, which has a formal Ir^{4+}-Ir^{4+} bond order of one, in comparison to $CaPtO_3$ for which the Pt^{4+}-Pt^{4+} bond order is zero. This analysis predicts that $CaReO_3$ post-perovskite (Re^{4+} radius = 0.63 Å) should also be accessible (but initial syntheses up to 25 GPa and 1400 K have not proved successful). As the stability conditions for post-perovskite oxides are rather severe, it is useful to explore solid solutions between these end-members to increase the range of available materials.

This study has demonstrated that the full series of $CaIr_{1-x}Pt_xO_3$ solid solutions can be stabilised, and the recovery of $CaIr_{0.5}Rh_{0.5}O_3$ suggests that the $CaIr_{1-x}Rh_xO_3$ series should also be accessible. However, the synthesis pressures (~15 GPa) required to give near-homogenous $CaIr_{1-x}Pt_xO_3$ solid solutions were found to be far higher than those to prepare the end-members (1 bar and 4 GPa for x = 0 and 1, respectively). Although x-ray diffraction, EDX analysis and Raman spectroscopy indicate that the $CaIr_{1-x}Pt_xO_3$ samples are homogenous, the magnetic measurements show that traces of $CaIrO_3$ are present.

A pronounced grain growth in the [100] direction is observed for all the samples in this study. This growth gives rise to a large preferred orientation even in loosely packed powders, and anchoring the particles on a greased surface was required to give XRD data suitable for structure

analysis. To the first approximation, no structural change is expected across the $CaIr_{1-x}Pt_xO_3$ series as Ir^{4+} and Pt^{4+} have identical ionic radii of 0.625 Å. However, some small changes in the lattice parameters and volume are observed experimentally, with evidence for possible local Ir/Pt order from the curvature in the c-parameter variation. The MO_6 octahedra are intrinsically distorted due to the anisotropic connectivity in the post-perovskite arrangement, but the loss of Jahn-Teller effects reduces the distortion of the MO_6 octahedra as x increases in the $CaIr_{1-x}Pt_xO_3$ series.

The electronic ground state of $CaIrO_3$ appears unconventional as the bulk electronic behaviour is semiconducting but the high temperature susceptibility has a temperature-independent variation. This could indicate an intrinsic Pauli paramagnetic and metallic behaviour, masked by resistive grain boundaries in the ceramic samples. Alternatively, the ground state may be gapped, with Ir-Ir bonding and spin-orbit coupling effects resulting in a near-zero Ir^{4+} magnetic moment. Strong spin-orbital coupling has been reported in Sr_2IrO_4.[24] The small ferromagnetic moment of 0.04 μ_B could be consistent with Stoner magnetism in a marginally metallic state, or canted order of larger, localised moments. Curie-Weiss paramagnetism emerges as $CaIrO_3$ is doped with non-magnetic Pt^{4+} or magnetic Rh^{4+} which suggests that disruption of a narrow Ir-Ir bonding band may be the dominant effect. The Curie transition is suppressed to zero at $x \approx 0.4$ for Pt-doping (assuming a linear $T_C(x)$ variation) but $CaIr_{0.5}Rh_{0.5}O_3$ has $T_C = 40$ K showing a clear dependence of the suppression on the magnetic nature of the dopants. The 290 K resistivity of $CaIr_{0.5}Pt_{0.5}O_3$ is six orders of magnitude greater than for $CaIrO_3$ whereas that of $CaIr_{0.5}Rh_{0.5}O_3$ is almost unchanged, consistent with the loss of hole carriers in the Ir d-band through Pt-doping.

Post-perovskite $CaIrO_3$ is also notable for having a very large magnetic anisotropy, comparable to that of hard magnetic materials such as $Nd_2Fe_{14}B$. This demonstrates that permanent magnets could be made from post-perovskites containing transition metals with larger spins.

Acknowledgements

We thank EPSRC and the Leverhulme Trust for support.

References

[1] Murakami, M; Hirose, K; Kawamura, K; Sata, K; Ohishi, Y *Science*, 2004, 304, 855-858

[2] Shim, S; Bengtson, A; Morgan, D; Sturhahn, W; Catalli, K; Zhao, J; Lerche, M; Prakapenka, V.B. *PNAS*, **2009**, *106*, 5508-5512

[3] Santilla´n, J; Shim, S; Shen, G; Prakapenka, V.B. *Geophys. Res. Lett.*, **2006**, *33*, L15307

[4] Hirai, S; Welch, M.D; Aguado, F; Redfern, S.A.T *Z. Kristallogr.*, **2009**, *224*, 345-350

[5] Ohgushi, K; Matsushita, Y; Miyajima, N; Katsuya, Y; Tanaka, M; Izumi, F; Gotou, H; Ueda, Y; Yagi, T *Physics and Chemistry of Minerals*, **2008**, *35*, 189-195

[6] Yamaura, K; Shirako, Y; Kojitani, H; Arai, M; Young, D.P.; Akaogi, M; Nakashima, M; Katsumata, T; Inaguma, Y; Takayama-Muromachi, E *J. Am. Chem. Soc.*, **2009**, *131*, 2722-2726

[7] Kojitani, H; Shirako, Y; Akaogi, M *Physics of the Earth and Planetary Interiors*, **2007**, *165*, 127–134

[8] Kojitani, H; Furukawa, A; Akaogi, M *Am. Mineral.*, **2007**, *92*, 229-232

[9] Inaguma, Y; Hasumi, K; Yoshida, M; Ohba, T; Katsumata, T *Inorg. Chem.*, **2008**, *47*, 1868-1870

[10] Hustoft, J; Shim, S; Kubo, A; Nishiyama, N *Am. Mineral.*, **2008**, *93*, 1654–1658

[11] Lindsay-Scott, A; Wood, I.G.; Dobson D.P.; Vo˘cadlo, L; Brodholt, J.P.; Crichton, W; Hanfland, M; Taniguchi, T *Physics of the Earth and Planetary Interiors*, **2010** to be published

[12] Ohgushi, K; Gotou, H; Yagi, T; Kiuchi, Y; Sakai, F; Ueda, Y *Phys. Rev. B*, **2006**, *74*, 241104

[13] Larson, A.C.; Von Dreele, R.B. *Los Alamos National Laboratory Report LAUR*, **2000**, 86-748

[14] Miyajima, N; Ohgushi, K; Ichihara, M; Yagi, T *Geophys. Res. Lett.*, **2006**, *33*, L12302

[15] Alonso, J.A.; Martinez-Lope, M.J.; Casais, M.T. *Inorg. Chem.*, **2000**, *39*, 917-923

[16] Von Dreele, R.B. *J.Appl. Crystallogr.*, **1997**, *30*, 517-525

[17] Nunes, W.C.; Folly, W.S.D; Sinnecker, J.P.; Novak, M.A. *Phys. Rev. B.*, **2004**, *70*, 014419

[18] Blundell, S *Magnetism in Condensed Matter*, **2001**, 128-136

[19] Haskel, D; Lang, J. C.; Islam, Z.; Cady, A; Srajer, G; Veenendaal, M; Canfield, P.C. *Phys. Rev. Lett.*, **2005**, *95*, 217207

[20] Shannon, R.D.; *Acta Cryst*., **1976**, A*32*, 751-767

[21] Grillo, M.E. *Comput. Mater. Sci.*, **2005**, *33*, 83-91

[22] Shimony, Y; Ben-dor, L *J. Mater. Sci. Lett.*, **1983**, *2*, 558-560

[23] Ivanovskii, A.L.; Chupakhina, T.I.; Zubkov, V.G; Tyutyunnik, A.P.; Krasilnikov, V.N.; Bazuev, G.V.; Okatov S.V.; Lichtenstein, A.I. *Phys. Lett. A*, **2005**, *348*, 66-70

[24] Kim, B.J.; Jin, H; Moon, S.J.; Kim, J.Y.; Park, B.G.; Leem, C.S.; Yu, J; Noh, T.W.; Kim,C; S.-J. Oh, S.J.; Park, J.H.; Durairaj, J; Cao, G; Rotenberg, E. *Phys. Rev. Lett.*, **2008**, *101*, 076402

Table 1: Frequencies of the five primary Raman modes of $CaIr_{1-x}Pt_xO_3$ and $CaIr_{0.5}Rh_{0.5}O_3$.

Frequency (cm^{-1})	$CaIrO_3$	$CaIr_{0.7}Pt_{0.3}O_3$	$CaIr_{0.5}Pt_{0.5}O_3$	$CaIr_{0.3}Pt_{0.7}O_3$	$CaIr_{0.5}Rh_{0.5}O_3$
ν_1	309	322	320	334	301
ν_2	444	452	451	452	449
ν_3	552	543	544	553	546
ν_4	-----	562	559	568	565
ν_5	712	688	692	703	648

Table 2: Average grain sizes and crystallographic results* for $CaIr_{1-x}Pt_xO_3$ and $CaIr_{0.5}Rh_{0.5}O_3$.

Compounds	$CaIrO_3$	$CaIr_{0.7}Pt_{0.3}O_3$	$CaIr_{0.5}Pt_{0.5}O_3$	$CaIr_{0.3}Pt_{0.7}O_3$	$CaIr_{0.5}Rh_{0.5}O_3$
Grain size (μm)	8.0	1.0	8.0	2.0	3.0
a (Å)	3.14592(4)	3.14114(7)	3.13575(7)	3.13216(4)	3.11997(6)
b (Å)	9.8635(1)	9.8795(2)	9.8924(1)	9.9051(1)	9.8652(1)
c (Å)	7.29903(9)	7.3081(1)	7.3169(1)	7.3303(1)	7.2930(1)
V ($Å^3$)	226.489(6)	226.795(12)	226.973(9)	227.420(7)	224.476(8)
R_{wp}	0.0560	0.0350	0.0359	0.0337	0.0634
χ^2	1.17	1.17	1.20	1.08	1.62
Ca: y	0.2503(3)	0.2474(6)	0.2510(5)	0.2500(4)	0.2484(4)
O1: y	0.425(1)	0.439(2)	0.429(2)	0.421(1)	0.441(2)
O2: y	0.1320(8)	0.127(1)	0.128(1)	0.1291(8)	0.132(1)
O2: z	0.4455(9)	0.451(2)	0.449(1)	0.450(1)	0.435(1)
U_{iso} ($Å^2$)	0.0024(5)	0.0131(6)	0.0009(5)	0.0037(6)	0.0077(9)
M-O1 (Å)	1.967(5) x2	1.923(5) x2	1.957(7) x2	1.993(5) x2	1.913(5) x2
M-O2 (Å)	2.081(5) x4	2.041(7) x4	2.053(7) x4	2.055(6) x4	2.087(7) x4
<M-O> (Å)	2.041(5)	1.999(6)	2.019(7)	2.032(6)	2.026(6)
M-O1 valence	0.77(1)	0.87(1)	0.80(2)	0.73(1)	0.87(1)
M-O2 valence	0.56(1)	0.63(1)	0.62(1)	0.62(1)	0.55(1)
BVS(Ir)	3.78(6)	4.26(6)	4.08(8)	3.94(6)	3.94(6)
M-O1-M (^{o})	136.1(7)	143.7(9)	138(1)	133.7(7)	145(1)
M-O2-M (^{o})	98.2(3)	100.6(5)	99.6(4)	99.3(4)	96.8(4)
O1-M-O2(^{o})	93.3(3)	91.3(4)	92.8(5)	94.5(3)	91.6(4)
O2-M-O2(^{o})	98.2(3)	100.6(5)	99.6(4)	99.3(4)	96.8(4)

*Atomic positions; Ca: 4c (0, y, 1/4), M = Ir/Pt/Rh: 4a (0, 0, 0), O1: 4c (0,y,1/4), O2: 8f (0, y, z); bond valences of M-O bonds were calculated as $\exp((d_i-d_0)/B)$ with d_0 values of 1.870 (Ir^{4+}-O^{2-}), 1.879 (Pt^{4+}-O^{2-}), 1.857 (Rh^{4+}-O^{2-}).

Table 3: Electronic and magnetic parameters of $CaIr_{1-x}Pt_xO_3$ and $CaIr_{0.5}Rh_{0.5}O_3$

Compounds	$CaIrO_3$	$CaIr_{0.7}Pt_{0.3}O_3$	$CaIr_{0.5}Pt_{0.5}O_3$	$CaIr_{0.3}Pt_{0.7}O_3$	$CaIr_{0.5}Rh_{0.5}O_3$
E_g (eV)	0.14	-	0.15	-	0.034
ρ_{290K} (Ωcm)	10.1	-	$8.37x10^6$	-	6.79
α (emu.mol^{-1})	0.00748(1)	0.00024(2)	0.00126(1)	0.00043(1)	0.00043(1)
θ (K)	-	37(11)	87(7)	39(8)	-16(12)
C (emu.K.mol^{-1})	-	0.053(9)	0.02(1)	0.031(7)	0.028(9)
μ_{eff} (μ_B/f.u.)	-	0.7(3)	0.4(3)	0.5(2)	0.5(3)
T_c (K)	108	20	-	-	40

Fig.1: Crystal structure of post-perovskite type $CaIrO_3$ showing layers of edge- and corner-sharing IrO_6 octahedra, separated by Ca ions.

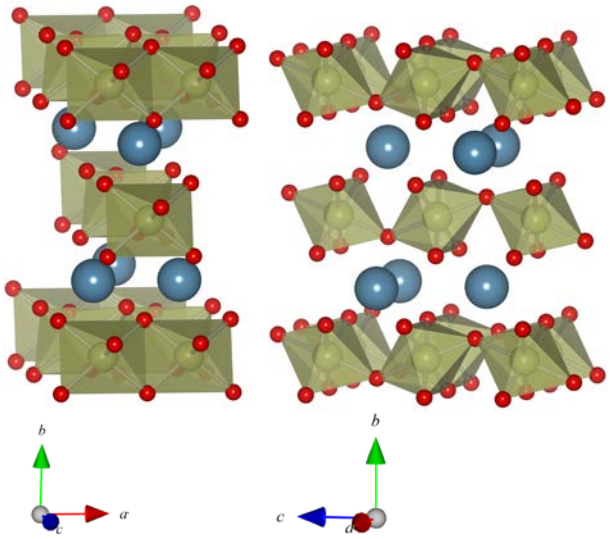
b
a
c
b
c
a

Fig.2: Fitted powder X-ray diffraction profiles of (a) $CaIrO_3$ and (b) $CaIr_{0.5}Pt_{0.5}O_3$ (upper/lower panels are for powdered samples on greased/ungreased holders, showing considerable texture effects in the latter).

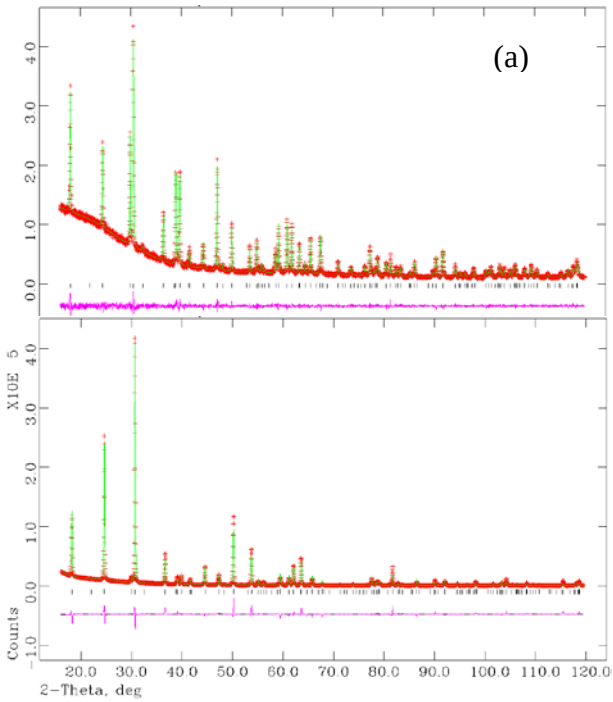

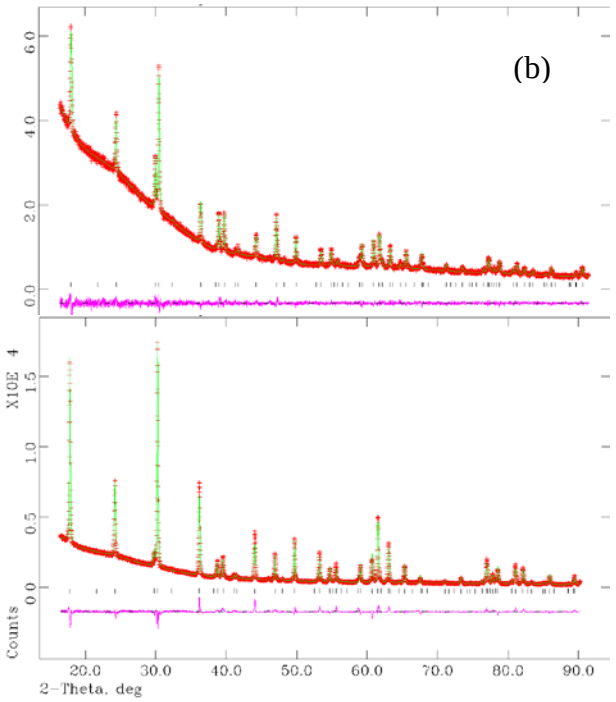

Fig.3: Typical SEM image of grains of $CaIr_{1-x}Pt_xO_3$ for (a) x = 0 (scale bar = 20 μm), (b) x = 0.3 (5 μm), (c) x = 0.5 (10 μm), (d) x = 0.7 (10 μm), and of (e) $CaIr_{0.5}Rh_{0.5}O_3$ (10 μm).

(a) (b)
(c) (d)
(e)

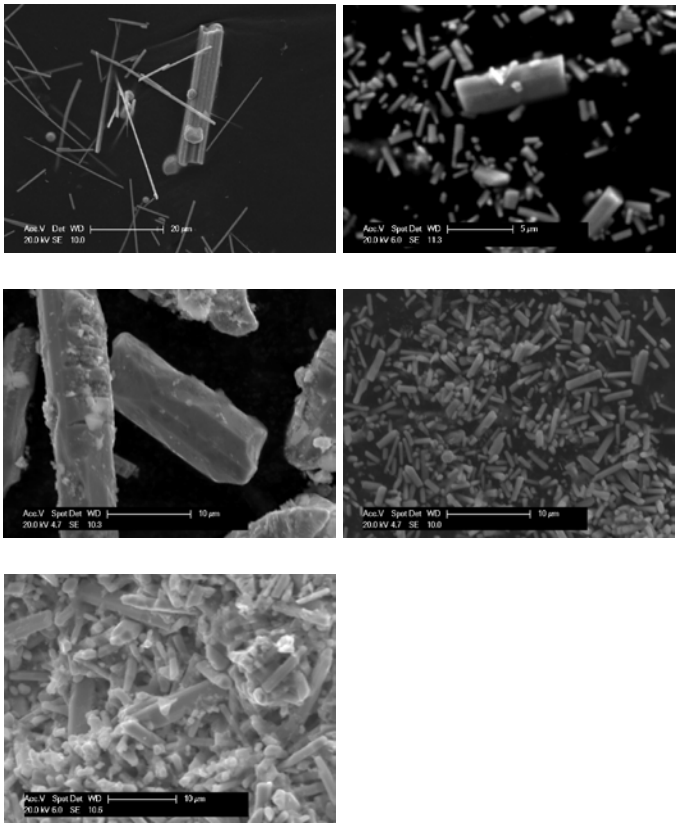

Fig. 4: Evolution of the orthorhombic lattice parameters, unit cell volume (V) and octahedral distortion parameter Δd, as defined in the text, for $CaIr_{1-x}Pt_xO_3$ solid solutions. The fitted curves are guides to the eye.

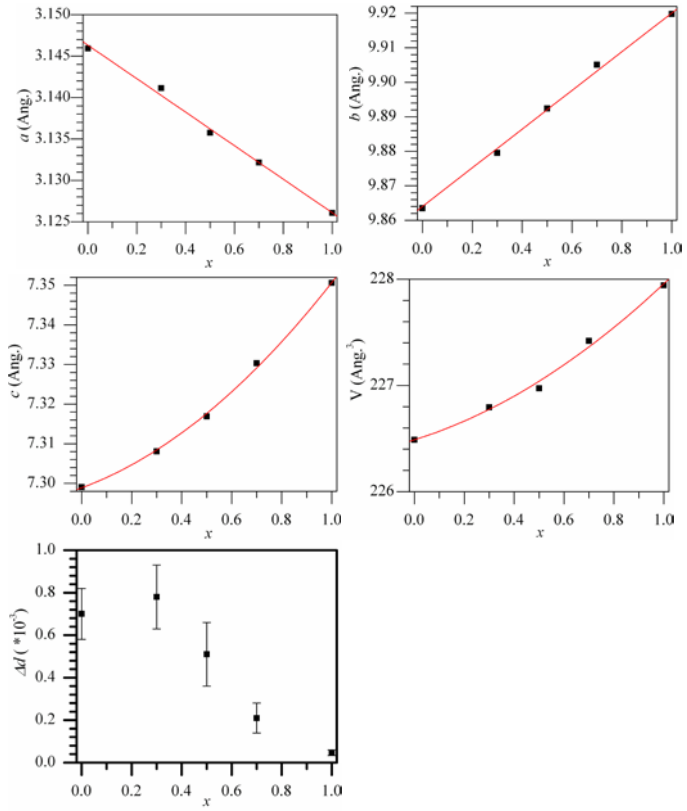

Fig. 5: Angular dependence of crystallite orientation density of $CaIr_{1-x}Pt_xO_3$ for (a) x = 0, (b) x = 0.3, (c) x = 0.5 (d) x = 0.7, and of (e) $CaIr_{0.5}Rh_{0.5}O_3$.

(a) (b)
(c) (d)
(e)

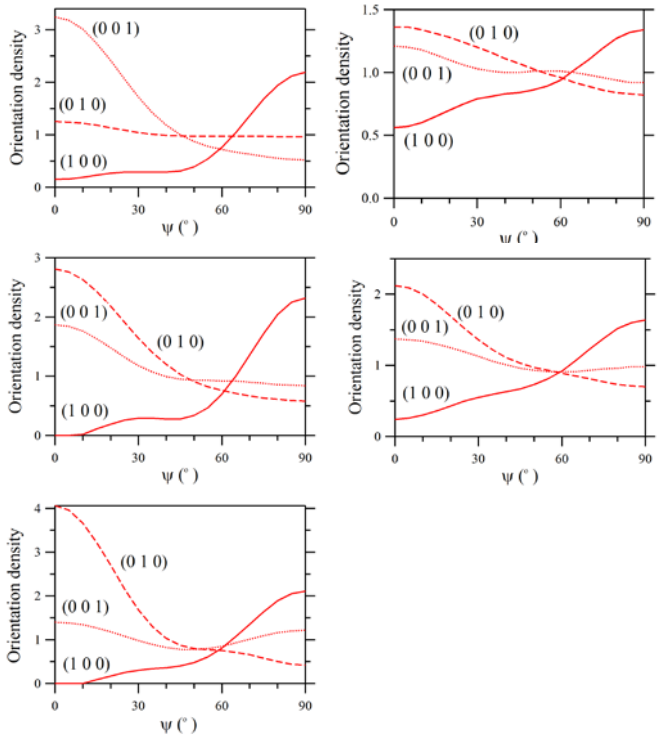

Fig.6: Temperature dependence of electrical resistivity for $CaIr_{0.5}Rh_{0.5}O_3$, $CaIrO_3$ and $CaIr_{0.5}Pt_{0.5}O_3$.

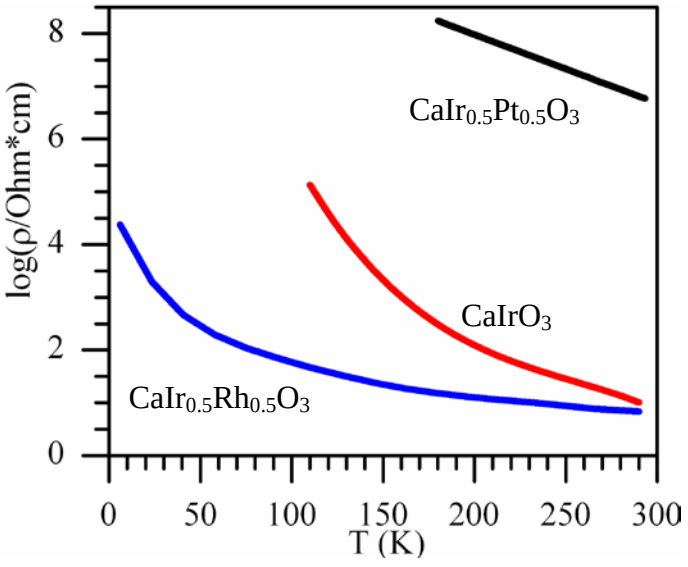

Fig.7: ZFC and FC (open and closed symbols) magnetic susceptibilities (M/H) of $CaIr_{1-x}Pt_xO_3$ for (a) x = 0, (b) x = 0.3, (c) x = 0.5, (d) x = 0.7, and of (e) $CaIr_{0.5}Rh_{0.5}O_3$. Insets show fits to inverse susceptibilities between 150 and 300 K.

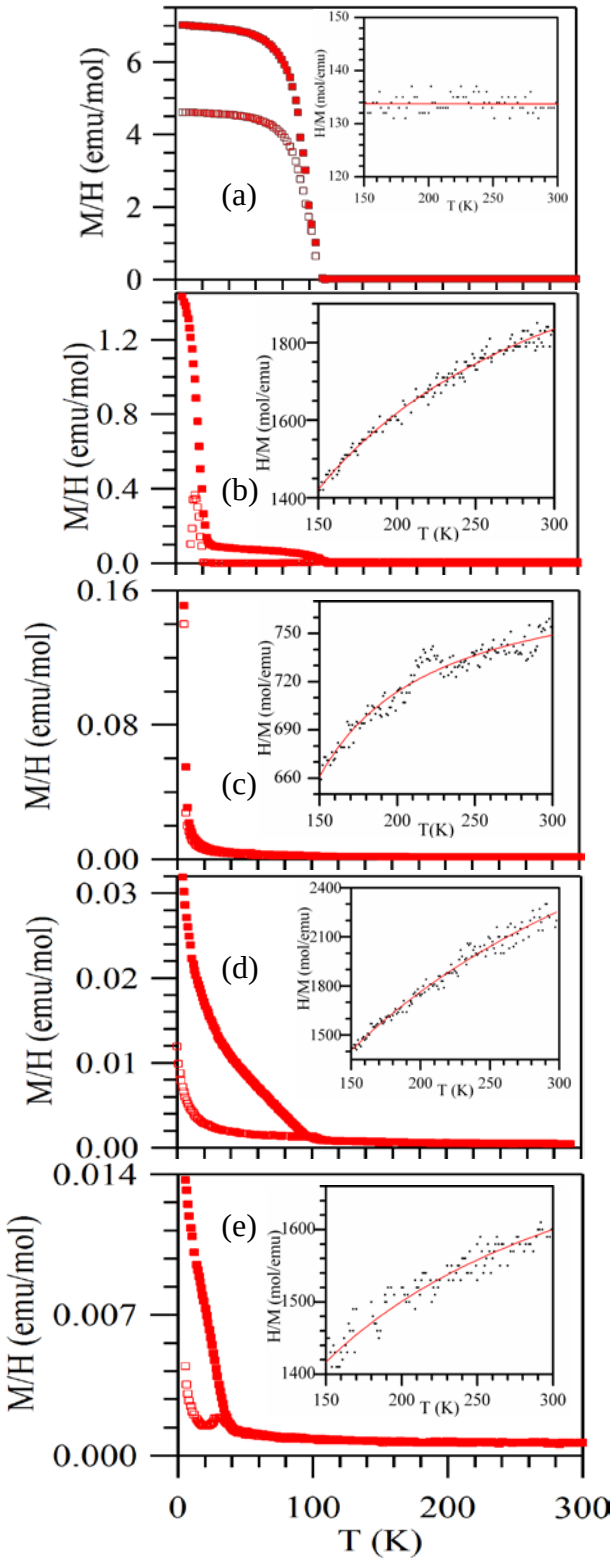

Fig.8: Magnetization-field hysteresis loops for (a) $CaIrO_3$ at temperatures between 5 and 105 K, (b) $CaIr_{0.7}Pt_{0.3}O_3$ at 5 K, and (c) $CaIr_{0.5}Rh_{0.5}O_3$ at 5 K.

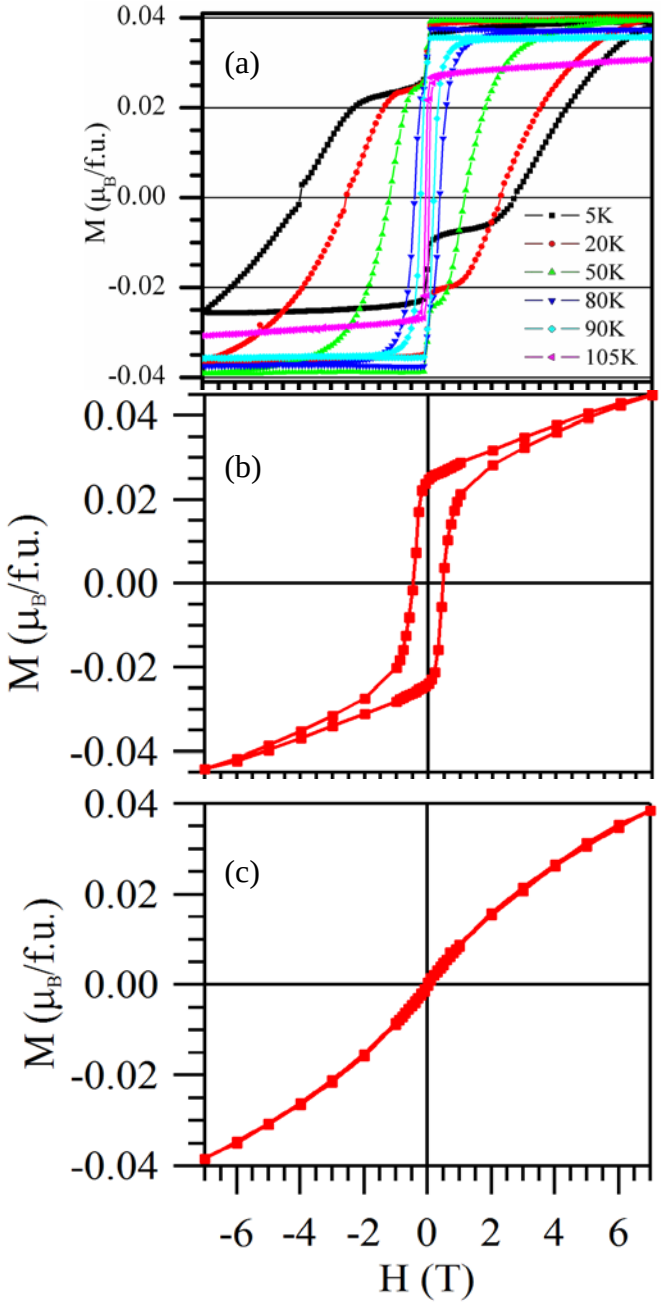

Fig.9: Temperature dependence of the coercive field for $CaIrO_3$ showing the fit described in the text.